Shape-Programmed Nanofabrication: Understanding the Reactivity of Dichalcogenide Precursors

Yijun Guo,[†,‡,§] Samuel R. Alvarado,[†,‡,§] Joshua D. Barclay,[†] and Javier Vela[†,‡,*]

[†]Department of Chemistry, Iowa State University, and [‡]Ames Laboratory, Ames, Iowa 50011, United States. [§]These authors contributed equally to this work.

ABSTRACT Dialkyl and diaryl dichalcogenides are highly versatile and modular precursors for the synthesis of colloidal chalcogenide nanocrystals. We have used a series of commercially available dichalcogenide precursors to unveil the molecular basis for the outcome of nanocrystal preparations, more specifically, how precursor molecular structure and reactivity affect the final shape and size of II–VI semiconductor nanocrystals. Dichalcogenide precursors used were diallyl, dibenzyl, di-*tert*-butyl, diisopropyl, diethyl, dimethyl, and diphenyl disulfides and diethyl, dimethyl, and diphenyl diselenides. We find that the presence of two distinctively reactive C–E and E–E bonds makes the chemistry of these precursors much richer and interesting than that of other conventional precursors such as the more common phosphine chalcogenides. Computational studies (DFT) reveal that the dissociation energy of carbon–chalcogen (C–E) bonds in dichalcogenide precursors (R–E–E–R, E = S or Se) increases in the order (R): diallyl < dibenzyl < di-*tert*-butyl < diisopropyl < diethyl < dimethyl < diphenyl. The dissociation energy of chalcogen–chalcogen (E–E) bonds remains relatively constant across the series. The only exceptions are diphenyl dichalcogenides, which have a much lower E–E bond dissociation energy. An increase in C–E bond dissociation energy results in a decrease in R–E–E–R precursor reactivity, leading to progressively slower nucleation and higher selectivity for anisotropic growth, all the way from dots to pods to tetrapods. Under identical experimental conditions, we obtain CdS and CdSe nanocrystals with spherical, elongated, or tetrapodal morphology by simply varying the identity and reactivity of the dichalcogenide precursor. Interestingly, we find that precursors with strong C–E and weak E–E bond dissociation energies such as Ph–S–S–Ph serve as a ready source of thiol radicals that appear to stabilize small CdE nuclei, facilitating anisotropic growth. These CdS and CdSe nanocrystals have been characterized using structural and spectroscopic methods. An intimate understanding of how molecular structure affects the chemical reactivity of molecular precursors enables highly predictable and reproducible synthesis of colloidal nanocrystals with specific sizes, shapes, and optoelectronic properties for customized applications.

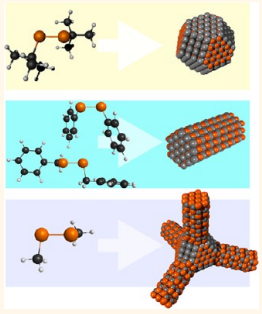

KEYWORDS: dichalcogenide precursors · bond dissociation energies · anisotropic structures · morphology control · selective growth

Dialkyl dichalcogenides (R–E–E–R; where R = alkyl or aryl, E = S, Se, or Te) recently re-emerged as highly versatile molecular precursors for the solution-phase synthesis of colloidal nanocrystals. Intriguingly, these dichalcogenides enable the isolation of metastable nanocrystalline phases with unusual composition and morphology. *t*Bu–E–E–*t*Bu (E = S or Se) precursors allow the isolation of $CuInE_2$ and Cu_2SnE_3 nanocrystals with metastable wurtzite phases.[1,2] A change in reaction solvent from oleylamine to squalene leads to $CuInE_2$ nanocrystals with the more stable chalcopyrite phase.[2,3] *t*Bu–S–S–*t*Bu serves as precursor to In_2S_3 nanorods[4] and $Cu_{2-x}S$ nanocrystals with a wide range of morphologies (from dots to dodecahedrons).[5] *t*Bu–Se–Se–*t*Bu serves as precursor to SnSe,[6] hexagonal BiSe,[7] and $Sn_xGe_{1-x}Se$ nanocrystals.[8] Photolysis of *t*Bu–Te–Te–*t*Bu in aqueous micellar conditions yields Te^0 nanorods.[9] Aqueous reaction of Me–Se–Se–Me with $SnCl_2$ in an autoclave yields SnSe nanosheets.[10] Ph–Se–Se–Ph allows the isolation of hexagonal and cubic nanocrystals of $CuInSe_2$ and $Cu_{2-x}S_ySe_{1-y}$.[11,12] Ph–Se–Se–Ph and Ph–Te–Te–Ph are useful alternatives to elemental chalcogenide precursors (Se or Te) in the synthesis of star-shaped SnTe and SnSe nanoparticles.[13] In spite of this very rich chemistry, it remains unclear what factors play a determinant role in the outcome of specific nanocrystal preparations.

Using the far more common phosphine chalcogenide precursors, we recently found that a single injection of premixed trioctylphosphine sulfide (Oct_3PS) and selenide (Oct_3PSe) to a bis-octadecylphosphonate

* Address correspondence to vela@iastate.edu.

Received for review February 4, 2013 and accepted March 21, 2013.

Published online March 21, 2013
10.1021/nn400596e

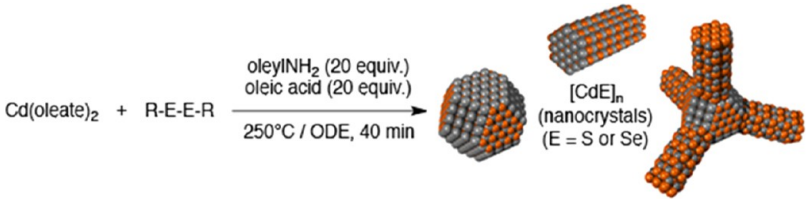

Scheme 1

cadmium complex ($Cd(ODPA)_2$) at 320 °C produces axially anisotropic $CdS_{1-x}Se_x$ nanorods characterized by having a thick, CdSe-rich "head" and a thin, CdS-rich "tail".[14,15] Using a combined experimental and computational approach, we showed that the time evolution and, formation mechanism and the S-to-Se content of these compositionally graded $CdS_{1-x}Se_x$ nanorods are direct consequences of relative phosphine chalcogenide precursor reactivity. Further, by tuning the sterics and electronics of a family of closely related $R_3P{=}E$ precursors (R = amide, alkyl, aryl or aryloxy; E = S or Se), we reproducibly and predictably synthesized CdE nanorods with controllable aspect (length-to-diameter) ratios between 10 and 100.[16] These observations open new avenues for achieving "bottom-up" molecular-level control of composition, morphology, and properties at the nanoscale.

Unlike phosphine chalcogenides ($R_3P{=}E$), which contain only one type of reactive bond (P═E), dichalcogenide precursors (R—E—E—R) contain two different types of reactive bonds (C—E and E—E). We were intrigued by the inherent modularity of these molecular precursors and wondered how varying the substituents (R = alkyl, aryl) around the reactive —E—E— unit could affect dichalcogenide precursor reactivity and, ultimately, the outcome of nanocrystal preparations. Experimentally, we observe that differently substituted dichalcogenides lead to completely different nanocrystal morphologies, some lead to dots, others to rods or tetrapods. The selectivity for such anisotropic structures is obviously affected by reaction parameters such as reaction time[17] and temperature,[18,19] precursor concentration,[20] medium acidity,[21] ligand type (amines,[22−24] halides,[52] phosphonic acids[25,26]) and chain length.[27,28] Commonly used methods to obtain II—VI and IV—VI rods and tetrapods include seeded growth,[29−32] continuous precursor injection,[33,34] and noninjection routes.[35] Dichalcogenides offer a unique system where the selectivity for anisotropic structures under identical experimental conditions can be directly traced back to the molecular structure and chemical reactivity of the molecular precursor used. Here we present the results of a combined experimental and computational study aimed at addressing this question.

RESULTS AND DISCUSSION

Seeking a deeper understanding of how molecular structure affects chemical precursor reactivity, we subjected different disubstituted dichalcogenides to a consistent set of nanocrystal forming conditions (Scheme 1). Briefly, we injected individual dichalcogenide precursors (1.1 equiv) to a freshly generated solution of $Cd(oleate)_2$ (0.40 mol), oleic acid (20 equiv), and oleylamine (20 equiv) in 1-octadecene (ODE) (4.6 mL) at 250 °C. At regular intervals, we took small equal aliquots from the reaction mixture and monitored nanocrystal evolution (nucleation, growth, and ripening) by optical spectroscopy. After 40 min at 250 °C, we isolated and fully characterized the nanocrystalline products. We repeated this procedure for several different commercially available dichalcogenides having different alkyl and aryl substituents.

Dichalcogenide Precursor Chemistry: A Springboard to Nanocrystal Shape Diversity. Our experimental observations show that, in general, dichalcogenide precursors that reacted quickly produced spherical nanocrystals, while those that reacted more slowly produced nanocrystals of nonspherical morphology (often tetrapods). Figure 1 shows the time evolution of UV—vis absorption spectra as well as final (after 40 min) TEM images of CdS nanocrystals obtained with different dialkyl disulfides (R—S—S—R). UV—vis spectroscopy shows the appearance of the first absorption (1*S*) peak characteristic of CdS nanocrystals within a few minutes for most precursors. Transmission electron microscopy (TEM) images show that some dichalcogenide precursors lead to the formation of CdS nanocrystals with a spherical morphology, while others lead to the formation of CdS nanocrystals with a tetrapod morphology.[36−38] The majority of spherical CdS nanocrystals (dots) have a zinc blende (cubic) structure, while the CdS tetrapods comprise wurtzite (hexagonal) arms extending from the {111} facets of zinc blende (cubic) cores (seeds) (see Supporting Information).[39−41] On the basis of these results, it is clear that the structure of the molecular precursor has considerable influence on the rate of growth, size, and morphology of the resulting nanocrystals.

Assessing the Strength of C—E and E—E Bonds from Computations. To better understand these observations, we computationally studied the different dichalcogenide precursors using the GAMESS software. We computed their carbon—chalcogen (C—E) and chalcogen—chalcogen (E—E) bond dissociation energies (BDEs, Scheme 2) using density functional theory (DFT) with the Boese—Martin Kinetics (BMK) functional, which has

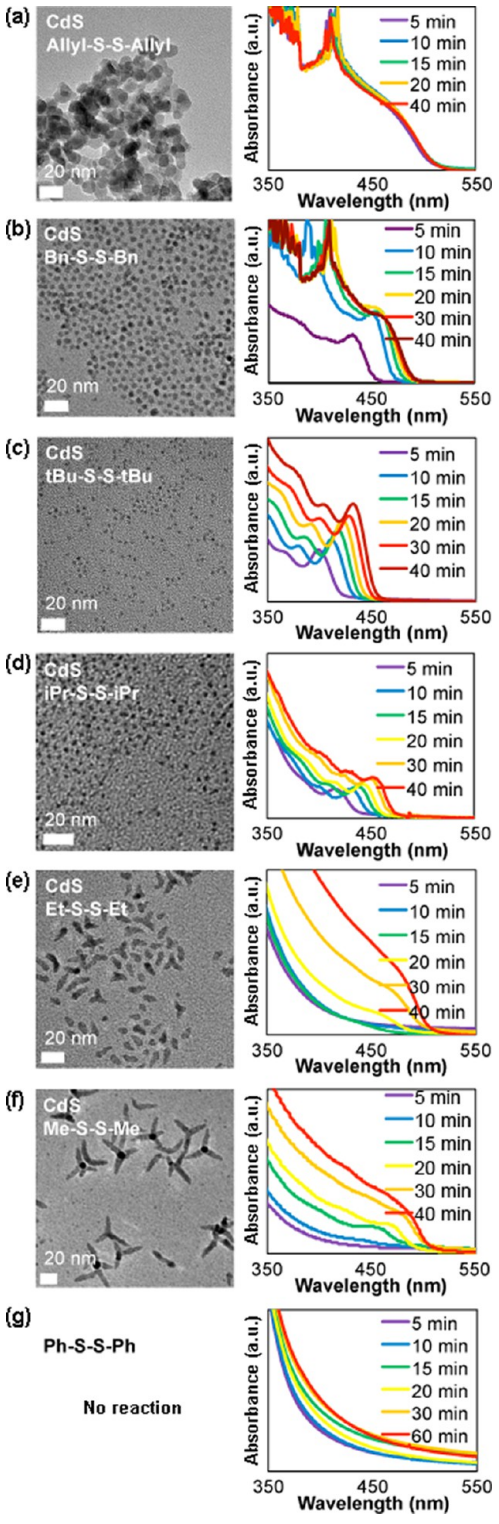

Figure 1. Representative TEM images after 40 min (left panel) and time evolution of UV−vis absorption spectra (right panel) of CdS nanocrystals obtained with (a) diallyl, (b) dibenzyl, (c) di-*tert*-butyl, (d) diisopropyl, (e) diethyl, and (f) dimethyl disulfide precursors. (g) Diphenyl disulfide was unreactive under identical conditions (0.40 mol $Cd(oleate)_2$, 1.1 equiv of R−S−S−R, 20 equiv of oleic acid, 20 equiv of oleylamine, 4.6 mL of ODE, 250 °C).

been shown to be a viable method to calculate thermodynamic properties such as BDEs at a lower

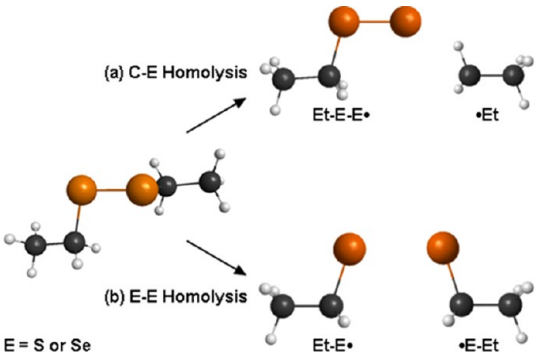

Scheme 2

computational cost than high-precision methods such as G3. Table 1 and Figure 2 show the computed BDEs of all precursors we investigated. Full computational results, including bond distances and dihedral angles, are available in the Supporting Information.

C−E and E−E BDEs: Comparison to Prior Experimental and Computational Data. In terms of absolute value, our computational results appear to underestimate the experimentally measured values reported previously for disubstituted dichalcogenides, particularly in the case of E−E BDEs. For example, laser photofragmentation time-of-flight mass spectrometric studies of Me−S−S−Me, •S−S−Me, and •S−Me yielded at 0 K a C−S BDE of 55.0 kcal/mol and a S−S BDE of 72.4 kcal/mol at 0 K,[42] compared to our calculated values of 59.03 and 58.04 kcal/mol, respectively (Table 1). This discrepancy could be due to either computational or experimental error. In terms of the trends observed, our computational results are in agreement with those observed experimentally. E−E BDEs measured experimentally are generally quoted in the range 51−72 kcal/mol;[43] those derived from calorimetry are 66.1 kcal/mol for Et−S−S−Et, 65.2 kcal/mol for Me−S−S−Me, and 51.2 kcal/mol for Ph−S−S−Ph,[44−48] compared to our calculated values of 59.48, 58.04, and 45.65 kcal/mol, respectively (Table 1). Our computational results compare well with previous calculations reported for disubstituted dichalcogenide compounds. Early computational references on C−S and S−S BDEs used a complete basis set approach instead of DFT.[49] High-level *ab initio* approaches using G3, G3B3, CBS-Q, CBS-4M, CCSD(T), and ROMP2 were applied to S−S BDEs.[50] A limited DFT study showed that the BMK functional provided accuracy close to composite methods, with S−S BDEs of 64.5 kcal/mol for *t*Bu−S−S−*t*Bu, 63.9 kcal/mol for *i*Pr−S−S−*i*Pr, 63.8 kcal/mol for Et−S−S−Et, 62.9 kcal/mol for Me−S−S−Me, and 48.3 kcal/mol for Ph−S−S−Ph.[51] These values and trends roughly agree (within 2−5 kcal/mol) with our computational results of 59.39, 59.69, 59.48, 58.04, and 45.65 kcal/mol, respectively. Further, all previous computations also find the S−S bond in Ph−S−S−Ph to be significantly weaker than

TABLE 1. Calculated Bond Dissociation (Homolysis) Energies (BDEs) for Dialkyl Dichalcogenide Precursors (R—E—E—R, E = S or Se) and Experimentally Observed Products from Their Reaction with Cd(oleate)$_2$[a]

precursor(s) R—E—E—R (E = S or Se)	C—E BDE (kcal/mol)	E—E BDE (kcal/mol)	(C—E)—(E—E) (kcal/mol)	40 min product morphology (1S peak)	size[b] (nm)
allyl—S—S-allyl	45.71	61.33	−15.62	nanocrystals[c] (480 nm)	9.4 ± 1.3
Bn—S—S—Bn	48.50	62.45	−13.94	manocrystals[c] (480 nm)	4.2 ± 0.6
*t*Bu—S—S—*t*Bu	52.81	59.39	−6.59	quantum dots[c] (430 nm)	2.2 ± 0.2
*i*Pr—S—S—*i*Pr	55.45	59.69	−4.24	quantum dots[c] (450 nm)	1.8 ± 0.3
Et—S—S—Et	58.13	59.48	−1.35	pods/multipods (470 nm)	pod length = 10.3 ± 2.8, pod width = 5.1 ± 0.6
Me—S—S—Me	59.03	58.04	+0.99	tetrapods (465 nm)	pod length = 19.5 ± 2.9, pod width = 5.5 ± 0.5
Ph—S—S—Ph	69.75	45.65	+24.11	no reaction (n.a.)	
Bn—S—S—Bn + Ph—S—S—Ph (1:1)	*d*	*d*	*d*	rods (470 nm)	rod length = 11.5 ± 1.5, rod width = 4.4 ± 0.5
*t*Bu—S—S—*t*Bu + Ph—S—S—Ph (1:1)	*d*	*d*	*d*	tetrapods (455 nm)	pod length = 24.1 ± 4.7, pod width = 3.5 ± 0.4
*i*Pr—S—S—iPr + Ph—S—S—Ph (1:1)	*d*	*d*	*d*	tetrapods (455 nm)	pod length = 21.3 ± 4.5, pod width = 2.3 ± 0.3
Et—Se—Se—Et[e]	52.01	56.41	−4.40	nanocrystals[c] (670 nm)	6.6 ± 0.6
Me—Se—Se—Me[f]	53.76	51.94	+1.82	multipod clusters (685 nm)	65.7 ± 13.1
Ph—Se—Se—Ph	64.44	43.63	+20.80	quantum dots[c] (550 nm)	3.5 ± 0.5

[a] Conditions: 0.40 mol Cd(oleate)$_2$, 1.1 equiv of R—E—E—R, 20 equiv of oleic acid, 20 equiv of oleylamine, 4.6 mL of ODE, 250 °C, 40 min (except [e]Et—Se—Se—Et, 10 min, [f]Me—Se—Se—Me, 5 min). [b] Average sizes (50—100 particles) ± one standard deviation. [c] Quantum dots have average diameters smaller than the Bohr radius reported for CdS (2.5—3.0 nm) or CdSe (5.4 nm).[64—66] [d] Not applicable (used a mixture of two precursors, see first column).

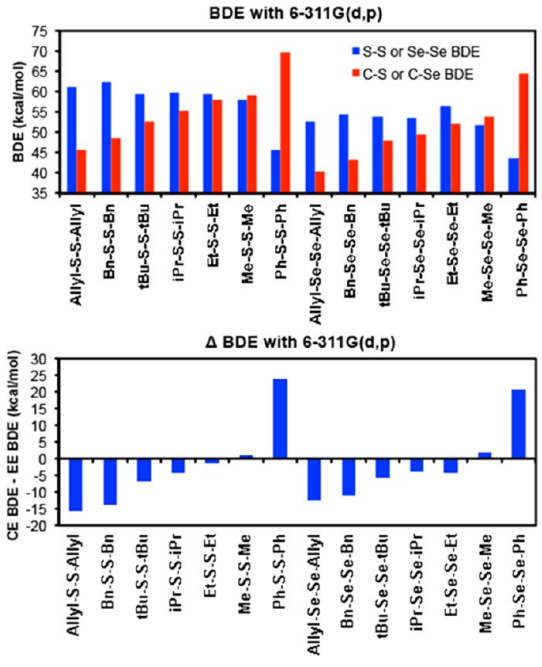

Figure 2. Bond dissociation (homolysis) energies (BDEs) calculated using density functional theory (DFT) with the Boese—Martin Kinetics (BMK) functional in GAMESS. Full computational results, including bond distances and dihedral angles, are available in the Supporting Information.

its C—S bond and the S—S bonds of other disulfides. DFT with different functionals other than BMK gave a Se—Se BDE of 51.8 kcal/mol for Me—Se—Se—Me, which compares well with our value of 51.94 kcal/mol.[52,53]

Assessing Dichalcogenide Precursor Reactivity from C—S BDEs. As shown in Table 1 and Figure 2, C—S bond energies progressively increase across the following series: allyl—S—S—allyl < Bn—S—S—Bn < *t*Bu—S—S—*t*Bu < *i*Pr—S—S—*i*Pr < Et—S—S—Et < Me—S—S—Me < Ph—S—S—Ph. In contrast, S—S bond energies remain roughly similar along most of the same series from allyl—S—S—allyl through Me—S—S—Me but significantly drop (by about one-third) for Ph—S—S—Ph. These trends greatly help understand our experimental observations. Both of the C—S bonds as well as the S—S bond must break in order to form nanocrystalline CdS. Because the strength of the S—S bond remains fairly constant among most disulfides, *the key factor that mainly determines the overall chemical reactivity of disulfide precursors is the strength of the C—S bond* (Figure 2 and Chart 1).

To illustrate, allyl—S—S—allyl and Bn—S—S—Bn have the *weakest C—S bonds* (45.71 and 48.50 kcal/mol, respectively) and are therefore the *most reactive precursors* in the series (Chart 1); they quickly (5—10 min) react with Cd(oleate)$_2$ to form large, non-quantum-confined spherical CdS nanocrystals (Figure 2). After 40 min, allyl—S—S—allyl and Bn—S—S—Bn lead to CdS particle sizes of 9.4 ± 1.3 and 4.2 ± 0.6 nm, respectively. In comparison, *t*Bu—S—S—*t*Bu and *i*Pr—S—S—*i*Pr have intermediate C—S bond strengths (52.81 and 55.45 kcal/mol, respectively) and are more mildly reactive; they react less quickly (5—40 min) with Cd(oleate)$_2$ to form small, quantum-confined spherical CdS nanocrystals (Figure 2). After 40 min, *t*Bu—S—S—*t*Bu and *i*Pr—S—S—*i*Pr lead to CdS particle sizes of 2.2 ± 0.2 and 1.8 ± 0.3 nm, respectively. For reference, the Bohr radius reported for CdS is between 2.5 and 3.0 nm.[54—56]

Further increasing the C—S bond strength and, with it, decreasing chemical precursor reactivity results in slower reaction and the selective formation of anisotropic structures. Et—S—S—Et and Me—S—S—Me have strong C—S bonds (58.13 and 59.03 kcal/mol, respectively) and are only weakly reactive; they react very slowly (20—40 min) and selectively with Cd(oleate)$_2$ to grow multipod and tetrapod structures

Chart 1

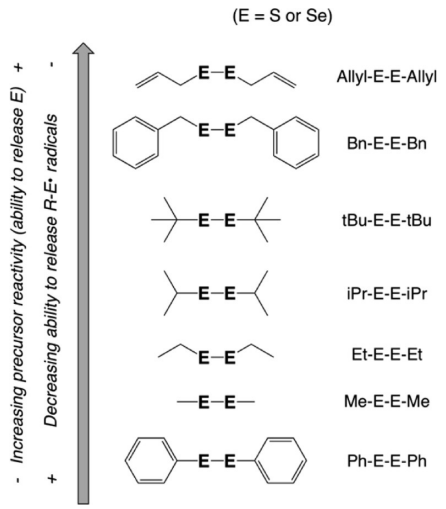

(Figure 2). After 40 min, Et−S−S−Et and Me−S−S−Me lead to CdS pods and tetrapods, respectively. For Et−S−S−Et, the average pod length and diameter are 10.3 ± 2.8 and 5.1 ± 0.6 nm, respectively. For Me−S−S−Me, the average pod length and diameter are 19.5 ± 2.9 and 5.5 ± 0.5 nm, respectively. At the end of the series and in stark contrast to all other dichalcogenides we tested, Ph−S−S−Ph has the *strongest C−S bond* (69.75 kcal/mol) and is *unreactive* (Chart 1); Ph−S−S−Ph alone (by itself) does not react with Cd(oleate)$_2$ under identical conditions to those used above for the other precursors (Figure 2).

Compared to the rest of the dichalcogenide precursors we used, Ph−S−S−Ph is different not only because it contains the strongest C−S bond (69.75 kcal/mol) but also because it contains the weakest S−S bond (45.65 kcal/mol). On the contrary, for most of the other dichalcogenides in the series, the calculated S−S bond is either stronger than or as strong as the calculated C−S bonds (Table 1 and Figure 2). Examination of the highest occupied (HOMO) and lowest unoccupied (LUMO) molecular orbital diagrams of diphenyl disulfide (Ph−S−S−Ph) reveals a strong overlap between the π orbital on the chalcogen atoms and the π orbital of the adjacent phenyl carbon (Figure 3). This $\pi-\pi$ overlap lends partial double bond character to the C−S bond, increasing the C−S bond strength (making it harder to break) and decreasing the C−S bond length (C−S 1.8085 Å for Ph−S−S−Ph *vs* C−S 1.8494−1.8721 Å for other disulfides; see Supporting Information). Other dialkyl dichalcogenides, such as diethyl disulfide (Et−S−S−Et), do not possess such overlap (Figure 3). On the basis of these differences, we hypothesized that the formation of anisotropic particles may arise from the relative ease (and rate) of C−S *versus* S−S bond breaking.

Understanding the Formation of Anisotropic Structures: Molecular Origin of Nanoscale Anisotropy. For allyl−S−S−allyl, Bn−S−S−Bn, *t*Bu−S−S−*t*Bu, and *i*Pr−S−S−*i*Pr, the C−S bonds are weaker than the S−S bond by at least 5 kcal/mol or more (Table 1 and Figure 2); therefore, by the time the S−S bond breaks in these precursors, the C−S bond has already broken, resulting in the release of S equivalents that can proceed to react with Cd(oleate)$_2$ to form spheroidal (0D) nanocrystals. In contrast, for Et−S−S−Et and Me−S−S−Me, the C−S

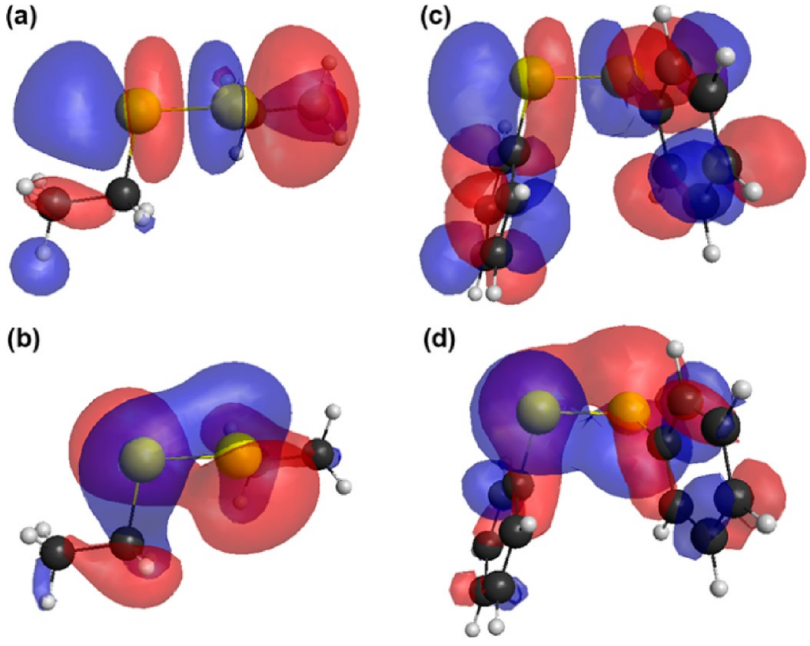

Figure 3. Lowest unoccupied (LUMO, top) and highest occupied (HOMO, bottom) molecular orbitals for Et−S−S−Et (a,b) and Ph−S−S−Ph (c,d) plotted with a contour value of 0.02. Calculated using density functional theory (DFT) with the Boese−Martin Kinetics (BMK) functional in GAMESS. Full computational results, including bond distances and dihedral angles, are available in the Supporting Information.

and S—S bonds are very similar in energy (only *ca.* 1.35—0.99 kcal/mol apart) (Table 1 and Figure 2); therefore, the C—S and S—S bonds break with similar ease and at roughly similar or comparable rates, resulting in the concomitant release of both S and R—S• radicals (Scheme 2). We expect thiol radicals of the form R—S• to act as excellent ligands due to their high affinity for soft cations and metal surfaces, for example, by binding at so-called "dangling bonds" or "surface traps".[57] The formation of radicals in these reactions is feasible given the high temperature (250 °C), long time (40 min), and nonpolar medium (octadecene and long chain surfactants) used here. Such harsh conditions are normally conducive to bond homolysis and radical chemistry. *In situ* generated R—S• radicals can act as capping ligands on the CdS surface, passivating the nanocrystals against further growth. Stabilizing and increasing the solution-phase lifetime of small, high-energy surface CdS nuclei could lead to slower and more selective nanocrystal growth, resulting in the formation of anisotropic structures such as the pods and tetrapods observed with Et—S—S—Et and Me—S—S—Me (Figure 1e,f). In fact, in the presence of excess O_2, a naturally occurring diradical, $Cd(oleate)_2$, and NaHSe react very slowly and selectively to produce anisotropic CdSe structures (nanowires).[58]

The above situation reverses for the Ph—S—S—Ph precursor, where the calculated C—S bond is much stronger than the calculated S—S bond by 24.11 kcal/mol (Table 1 and Figure 2). This explains the apparent lack of reactivity of Ph—S—S—Ph: the S—S bond breaks very easily, but the C—S bond does not, resulting in the facile release of R—S• radicals but not of S (Scheme 2). In fact, even though by itself it does not appear to react with $Cd(oleate)_2$, we reasoned that Ph—S—S—Ph should be extremely efficient at generating R—S• radicals. Because such thiol radicals can serve as surface-passivating ligands, we hypothesized that repeating CdS forming reactions using a mixture of the apparently "unreactive" Ph—S—S—Ph with a reactive dichalcogenide such as *t*Bu—S—S—*t*Bu or *i*Pr—S—S—*i*Pr should induce the formation of anisotropic structures. As noted above, reacting $Cd(oleate)_2$ with *t*Bu—S—S—*t*Bu or *i*Pr—S—S—*i*Pr normally results in CdS dots (Figure 1b,c). However, mixing any of these two precursors with Ph—S—S—Ph could mimic the situation where a very slowly reacting (and selective) precursor such as Et—S—S—Et or Me—S—S—Me is used; more specifically, *t*Bu—S—S—*t*Bu or *i*Pr—S—S—*i*Pr would serve as a source of S, while Ph—S—S—Ph would serve as a source of surface-stabilizing R—S• radicals.

Inducing Anisotropy: Testing the Role of *In Situ* Generated Thiol Radicals. Figure 4 shows representative data confirming this prediction: while Ph—S—S—Ph alone is unreactive against $Cd(oleate)_2$, and Bn—S—S-Bn alone leads to quick formation of CdS nanocrystals (Figure 4a,b), a 1:1 mixture of Bn—S—S—Bn and Ph—S—S—Ph leads to the sole, highly selective formation of CdS rods (Figure 4c). In turn, while *t*Bu—S—S—*t*Bu alone leads to quick CdS dot formation (Figure 4d), a 1:1 mixture of *t*Bu—S—S—*t*Bu and Ph—S—S—Ph leads to highly selective formation of CdS tetrapods (Figure 4e). Similarly, while *i*Pr—S—S—*i*Pr alone leads to quick CdS dot formation (Figure 4f), a 1:1 mixture of *i*Pr—S—S—*i*Pr and Ph—S—S—Ph leads to highly selective formation of CdS tetrapods. These reactions cleanly and reproducibly produce anisotropic CdS structures (only rods or tetrapods), without the need for any of the widespread and commonly used size- and/or shape-selective purification protocols. In addition, pod branching depends on the ratio of precursors used (for example, the amount of *t*Bu—S—S—*t*Bu compared to that of Ph—S—S—Ph; see Supporting Information).

These results strongly support and are consistent with our hypothesis above that *in situ* generated thiol radicals (R—S• radicals) serve as efficient surface-passivating ligands, increasing the lifetime of small CdS nuclei long enough to allow for slow (and selective) heterogeneous (epitaxial) growth of new CdS (pods). Dichalcogenide precursors with intermediate S—S and C—S bond strengths such as Et—S—S—Et and Me—S—S—Me are good at generating R—S• radicals, and they are also mild (slowly releasing) sources of S; therefore, these precursors are ideal for selective anisotropic growth (Figure 1e,f). With a much weaker S—S bond, the ability to generate R—S• radicals is even higher for Ph—S—S—Ph, but this precursor has a prohibitively strong C—S bond and is unable to serve as a source of S (Figures 1g and 4a); however, when mixed with other precursors that are good S sources such as Bn—S—S—Bn, *t*Bu—S—S—*t*Bu, or *i*Pr—S—S—*i*Pr, Ph—S—S—Ph allows the generation of anisotropic structures such as rods and tetrapods where usually only dots would form (Figure 4c,e,g). In these mixed precursor experiments, the degree of anisotropy is a direct result of an exquisite interplay between the ability of Ph—S—S—Ph to give off surface-stabilizing R—S• radicals and the chemical reactivity of a second precursor (namely, the latter's ability to give off S as measured by its relative C—S BDE). We are currently pursuing further mechanistic and spectroscopic studies that will help to better delineate the effect of *in situ* generated thiyl radicals on the rate of growth, shape selectivity, and overall outcome of colloidal nanocrystal preparations, and this will be the topic of a separate paper in the future.

Other Effects of Dichalcogenide Reactivity: Understanding Nucleation, Growth, and Ripening. Our calculations and experimental observations also help understand the relative rates of nucleation, growth, and ripening of CdS nanocrystals made with different dichalcogenides (Figure 5). As judged from the position of the first 1*S* absorption peak (Figure 5a),[59—62] Bn—S—S—Bn (C—S BDE 48.50 kcal/mol) reacts with $Cd(oleate)_2$ to form

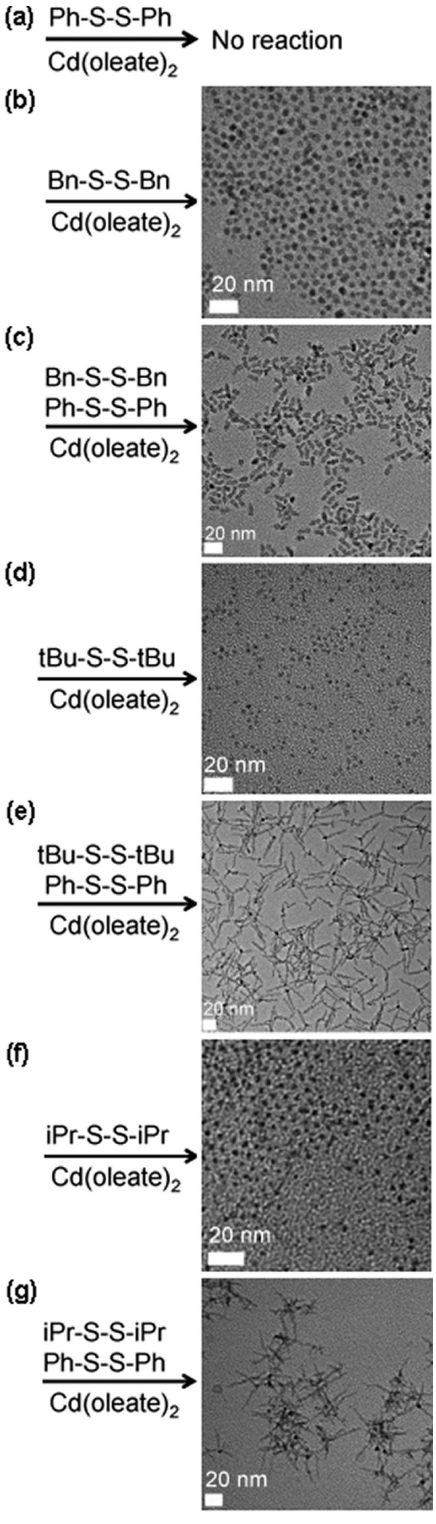

Figure 4. Under identical conditions (0.40 mol Cd(oleate)$_2$, 1.1 equiv of R−S−S−R, 20 equiv of oleic acid, 20 equiv of oleylamine, 4.6 mL of ODE, 250 °C): Ph−S−S−Ph is unreactive (a); Bn−S−S−Bn produces CdS dots while a 1:1 mixture of Bn−S−S−Bn and Ph−S−S−Ph produces CdS rods (c); *t*Bu−S−S−*t*Bu produces CdS dots (d) while a 1:1 mixture of *t*Bu−S−S−*t*Bu and Ph−S−S−Ph produces CdS tetrapods (e); *i*Pr−S−S−*i*Pr produces CdS dots (f) while a 1:1 mixture of *i*Pr−S−S−*i*Pr and Ph−S−S−Ph produces CdS tetrapods (g).

larger CdS nanocrystals than *t*Bu−S−S−*t*Bu (C−S BDE 52.81 kcal/mol) or *i*Pr−S−S−*i*Pr (C−S BDE 55.45 kcal/mol). Interestingly, increasing the initial dichalcogenide concentration also results in an increase in the size of the CdS nanocrystals (*i*Pr−S−S−*i*Pr (×2) *vs* *i*Pr−S−S−*i*Pr in Figure 5a). These observations suggest that *the rate of nanocrystal growth* (heterogeneous nucleation of new CdS material epitaxially on existing CdS particles)[63] *is directly dependent on dichalcogenide reactivity and concentration*. Dividing the CdS particle size (derived from the position of the 1*S* peak) by its size-specific absorption coefficient or "cross section" (ε) is proportional to the number of CdS particles present in the reaction at any given time (Figure 5b).[68−71] Interestingly, reaction of Cd(oleate)$_2$ with Bn−S−S−Bn (C−S BDE 48.50 kcal/mol) initially forms approximately twice as many initial nuclei as *t*Bu−S−S−*t*Bu (C−S BDE 52.81 kcal/mol) and *ca.* 7 times as many nuclei as *i*Pr−S−S−*i*Pr (C−S BDE 55.45 kcal/mol) (short reaction times ≤5 min, Figure 5b). However, increasing the initial dichalcogenide concentration does not affect the number of initially formed CdS nuclei (*i*Pr−S−S−*i*Pr (×2) *vs* *i*Pr−S−S−*i*Pr in Figure 5b). Therefore, *the rate of nanocrystal nucleation* (homogeneous nucleation of new CdS nuclei) *is extremely sensitive to, and directly dependent on, the reactivity of the dichalcogenide precursor used but not its concentration*. Once the initial nucleation event has occurred, the change

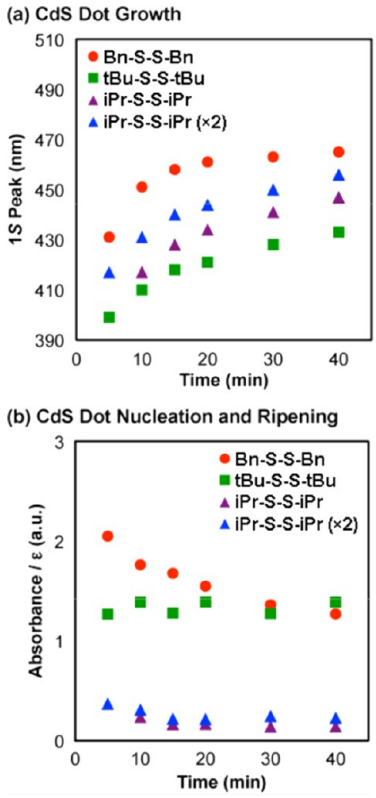

Figure 5. Time evolution of particle size (growth, a) and number of nuclei and ripening (b) of CdS nanocrystals produced with different dialkyl dichalcogenide precursors under similar reaction conditions (0.40 mol Cd(oleate)$_2$, 1.1 equiv of R−S−S−R, 20 equiv of oleic acid, 20 equiv of oleylamine, 4.6 mL of ODE, 250 °C).

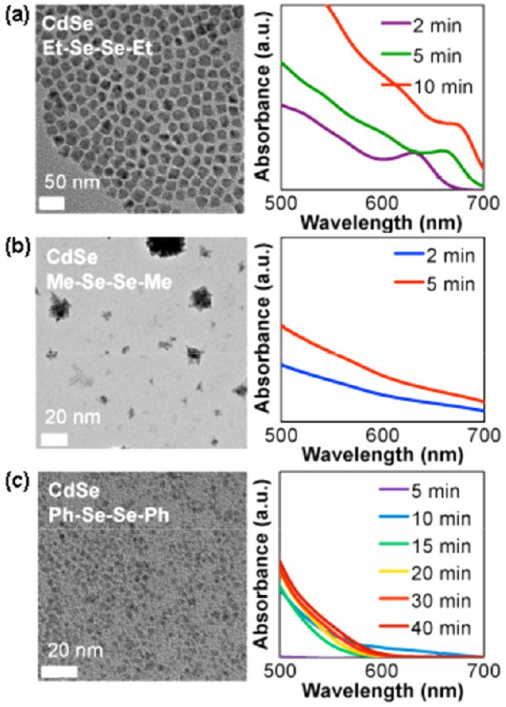

Figure 6. Representative TEM images (left panel) and time evolution of UV–vis absorption spectra (right panel) of CdS nanocrystals obtained with (a) diethyl (10 min), (b) dimethyl (5 min), and (c) diphenyl disulfide (40 min) precursors under identical conditions (0.40 mol $Cd(oleate)_2$, 1.1 equiv of R–Se–Se–R, 20 equiv of oleic acid, 20 equiv of oleylamine, 4.6 mL of ODE, 250 °C).

in the number of CdS particles over time (*i.e.*, *ripening*) does not appear to be directly affected by precursor reactivity but rather appears to be a simple consequence of the initial CdS particle size (Figure 5b).

Comparing Diselenide with Disulfide Precursors. The diselenide precursors reacted more quickly than the analogous disulfide precursors. We previously observed similar behavior in trialkylphosphine chalcogenide precursors ($R_3P{=}E$, E = Se *vs* S),[14−16] and we attribute this difference to the fact that Se forms weaker and longer (C–E and E–E) bonds compared to S (see Supporting Information). Et–Se–Se–Et has weak C–Se bonds (52.01 kcal/mol) and reacts quickly with $Cd(oleate)_2$ to form CdSe quantum dots in <2 min; these become non-quantum-confined CdSe nanocrystals with a particle size of 6.6 ± 0.6 nm after 10 min (Figure 6a). For reference, the Bohr radius reported for CdSe is *ca.* 5.4 nm.[42] Me–Se–Se–Me has stronger C–Se bonds (53.76 kcal/mol) and reacts more slowly and selectively with $Cd(oleate)_2$ to form CdSe multipods; these show significant clustering after 5 min (Figure 6b). Ph–Se–Se–Ph has even stronger C–Se bonds (64.44 kcal/mol) and barely reacts with $Cd(oleate)_2$ to form very small CdSe quantum dots (Figure 6c). We attribute the difference between Ph–S–S–Ph (unreactive) and Ph–Se–Se–Ph (marginally reactive) to the difference in C–E bond dissociation energies between these two precursors (C–S BDE 69.75 kcal/mol in Ph–S–S–Ph *vs* C–Se BDE 64.44 kcal/mol in Ph–Se–Se–Ph) (Table 1). Thus, although more reactive, the diselenide (R–Se–Se–R) precursors show similar reactivity patterns as those observed for the disulfide (R–S–S–R) precursors above.

CONCLUSION

By studying a variety of commercially available dichalcogenides and the outcome of their solution-phase reaction with a cadmium oleate complex under identical conditions, we have demonstrated that the formation and degree of anisotropy of different nanocrystalline products can be traced back to the precise molecular structure, bonding energetics, and chemical reactivity of the different dichalcogenides used. Using DFT, we showed that the main factor that determines overall dichalcogenide precursor reactivity is the carbon–chalcogen (C–S or C–Se) bond dissociation energy, while the chalcogen–chalcogen (S–S or Se–Se) bond dissociation energy remains more or less constant across a series of dichalcogenides (disulfides or diselenides). The only exceptions to this trend are diphenyl dichalcogenides, which exhibit the weakest chalcogen–chalcogen bond and the strongest carbon–chalcogen bond due to strong π orbital interaction between the first carbon atom in the phenyl ring and the adjacent chalcogen atom. The presence of this strong C–S bonding interaction causes Ph–S–S–Ph to appear unreactive when used alone. Conversely, allyl–S–S–allyl has the weakest C–S bond and reacts quickly to produce large aggregated CdS nanocrystals. Similar trends in bond dissociation energies and reactivity hold for the diselenide precursors, although their longer and weaker bonds lead to increased reactivity and more aggregated particles compared to disulfide precursors.

To understand the formation of anisotropic structures from disulfides containing roughly equal C–S and S–S bond strengths (Et–S–S–Et or Me–S–S–Me), we carried out reactions employing 1:1 mixtures of a thiol radical source (Ph–S–S–Ph) and a sulfur monomer source (Bn–S–S–Bn, *t*Bu–S–S–*t*Bu, or *i*Pr–S–S–*i*Pr). Ph–S–S–Ph by itself yielded no nanocrystalline products, and the sulfur sources alone yielded only spherical nanocrystals. However, the mixed precursor experiments resulted in the exclusive formation of anisotropic structures (rods or tetrapods). Our present hypothesis is that the disulfide bond of Ph–S–S–Ph homolyzes to produce PhS• radicals which passivate and stabilize small zinc blende CdS nuclei. These core nuclei arise from the reaction between the second sulfur (Bn–S–S–Bn, *t*Bu–S–S–*t*Bu, or *i*Pr–S–S–*i*Pr) and cadmium precursors, which can then slowly and selectively grow wurtzite arms on the {111} facets of the initial zinc blende cores. Our computations shed light on the experimentally observed rates of nucleation, growth, and ripening of CdS nanocrystals. The rates of CdS nanocrystal nucleation and growth are directly

dependent on dichalcogenide chemical reactivity or inversely proportional to C−S bond strength. Increasing the initial dichalcogenide concentration increases CdS nanocrystal size but does not affect the number of CdS particles already present after the initial nucleation stage. This implies that the observed sizes and morphology are not a function of precursor concentration but only its characteristic reactivity. By applying our understanding of the chemistry of molecular precursors, we may begin to rationalize and predict desirable nanocrystalline properties such as morphology, composition, and optoelectronic properties. This "bottom-up" approach to controllable and predictable nanocrystal synthesis allows for the preparation of a diverse array of morphologies based on fundamental, tangible, and measurable molecular properties such as bond energies. We believe this and similar efforts will lead to the reliable syntheses of colloidal nanomaterials for customized applications.

METHODS

Materials. Cadmium oxide (CdO, 99.998%) and oleic acid (90%) were purchased from Alfa Aesar; diallyl disulfide (allyl−S−S−allyl, 80%), dibenzyl disulfide (Bn−S−S−Bn, 98%), di-*tert*-butyl disulfide (*t*Bu−S−S−*t*Bu, 97%), diisopropyl disulfide (*i*Pr−S−S−*i*Pr, 96%), diethyl disulfide (Et−S−S−Et, 99%), dimethyl disulfide (Me−S−S−Me, 99%), and dimethyl diselenide (Me−Se−Se−Me, 96%) from Sigma-Aldrich; diphenyl disulfide (Ph−S−S−Ph, 99%), 1-octadecene (ODE, 90%), and oleylamine (80−90%) from Acros; diethyl diselenide (Et−Se−Se−Et) and diphenyl diselenide (Ph−Se−Se−Ph, 98%) from Strem.

Synthesis. *Dichalcogenide Addition Solution.* Inside a glovebox filled with dry N_2, the dichalcogenide precursor (0.42 mmol) (61.0 mg of allyl−S−S−allyl, 104 mg of Bn−S−S−Bn, 75.0 mg of *t*Bu−S−S−*t*Bu, 63.1 mg of *i*Pr−S−S−*i*Pr, 51.0 mg of Et−S−S−Et, 39.6 mg of Me−S−S−Me, 91.0 mg of Et−Se−Se−Et, 79.0 mg of Me−Se−Se−Me, or 131 mg of Ph−Se−Se−Ph) was thoroughly dissolved in ODE (1.00 g, 1.27 mL) to afford a homogeneous mixture. *Cadmium chalcogenide particles.* Inside a three-neck flask, CdO (51.2 mg, 0.40 mmol), oleic acid (2.24 g, 8.00 mmol), oleylamine (2.14 g, 8.00 mmol), and ODE (2.62 g, 3.32 mL) were degassed under vacuum at 80 °C for 30 min, refilled with Ar, and heated to 180 °C for 10 min until the mixture became a homogeneous, optically clear solution. The solution was cooled to 80 °C, degassed under vacuum at 80 °C for 30 min, refilled with Ar, and heated to 250 °C. After 5 min, the dichalcogenide addition solution (above) was quickly injected. Aliquots (0.10 mL) were taken at different times, added to the same amount of toluene (3 mL) every time, and analyzed by UV−vis absorption and PL. After 40 min (disulfides) or 5−40 min (diselenides), the mixture was allowed to cool to room temperature. Nanocrystals were isolated and purified twice by washing with a 1:2 v/v acetone/methanol mixture and centrifugation at 4900 rpm for 5 min.

Optical Characterization. Absorption spectra were measured with a photodiode array Agilent 8453 UV−vis spectrophotometer. Steady-state PL spectra were measured with a Horiba-Jobin Yvon Nanolog scanning spectrofluorometer equipped with a photomultiplier detector.

Structural Characterization. *Powder X-ray Diffraction.* XRD was measured using Cu Kα radiation on a Scintag XDS-2000 diffractometer. *Transmission Electron Microscopy* (TEM) was conducted on carbon-coated copper grids using a FEI Technai G2 F20 field emission scanning transmission electron microscope (STEM) at 200 kV (point-to-point resolution <0.25 nm, line-to-line resolution <0.10 nm). *Particle dimensions* were measured manually and/or with ImageJ for >50−100 particles. Averages are reported ± one standard deviation.

Computational Methods. Bond dissociation energies (BDEs) were calculated using GAMESS[64,65] at the DFT[66] level of theory with the BMK (Boese−Martin Kinetics) functional,[67] which has been shown to provide accuracy near that of high-precision complete basis set (CBS) methods.[68,69] Geometries were optimized using the 6-31G(d) basis set[70] followed by single-point calculations with the 6-311G(d,p) basis set[71] to determine BDEs.[72] Frequency calculations were performed to obtain zero point energies and enthalpies at 273 K and to ensure that the Hessian matrices of the optimized geometries contained no negative eigenvalues.[73]

Conflict of Interest: The authors declare no competing financial interest.

Acknowledgment. J.V. thanks Iowa State University for start-up funds. S.R.A. thanks ISU's Graduate College for a George Washington Carver Doctoral Fellowship. S.R.A. and J.V. thank Hua-Jun Fan, Jakoah Brgoch, Theresa Windus, and Mark Gordon for helpful discussions.

Supporting Information Available: Additional table and figures. This material is available free of charge *via* the Internet at http://pubs.acs.org.

REFERENCES AND NOTES

1. Norako, M. E.; Franzman, M. A.; Brutchey, R. L. Growth Kinetics of Monodisperse Cu−In−S Nanocrystals Using a Dialkyl Disulfide Sulfur Source. *Chem. Mater.* **2009**, *21*, 4299–4304.
2. Norako, M. E.; Brutchey, R. L. Synthesis of Metastable Wurtzite $CuInSe_2$ Nanocrystals. *Chem. Mater.* **2010**, *22*, 1613–1615.
3. Norako, M. E.; Greaney, M. J.; Brutchey, R. L. Synthesis and Characterization of Wurtzite-Phase Copper Tin Selenide Nanocrystals. *J. Am. Chem. Soc.* **2012**, *134*, 23–26.
4. Franzman, M. A.; Brutchey, R. L. Solution-Phase Synthesis of Well-Defined Indium Sulfide Nanorods. *Chem. Mater.* **2009**, *21*, 1790–1792.
5. Li, W.; Shavel, A.; Guzman, R.; Rubio-Garcia, J.; Flox, C.; Fan, J.; Cadavid, D.; Ibáñez, M.; Arbiol, J.; Morante, J. R.; *et al.* Morphology Evolution of $Cu_{2-x}S$ Nanoparticles: From Spheres to Dodecahedrons. *Chem. Commun.* **2011**, *47*, 10332–10334.
6. Franzman, M. A.; Schlenker, C. W.; Thompson, M. E.; Brutchey, R. L. Solution-Phase Synthesis of SnSe Nanocrystals for Use in Solar Cells. *J. Am. Chem. Soc.* **2010**, *132*, 4060–4061.
7. Webber, D. H.; Brutchey, R. L. Photochemical Synthesis of Bismuth Selenide Nanocrystals in an Aqueous Micellar Solution. *Inorg. Chem.* **2011**, *50*, 723–725.
8. Buckley, J. J.; Rabuffetti, F. A.; Hinton, H. L.; Brutchey, R. L. Synthesis and Characterization of Ternary $Sn_xGe_{1-x}Se$ Nanocrystals. *Chem. Mater.* **2012**, *24*, 3514–3516.
9. Webber, D. H.; Brutchey, R. L. Photolytic Preparation of Tellurium Nanorods. *Chem. Commun.* **2009**, 5701–5703.
10. Kang, S.-K.; Jia, L.; Li, X.; Yin, Y.; Li, L.; Guo, Y.-G.; Mu, J. Amine-Free Preparation of SnSe Nanosheets with High Crystallinity and Their Lithium Storage Properties. *Colloids Surf., A* **2012**, *406*, 1–5.
11. Wang, J.-J.; Xue, D.-J.; Guo, Y.-G.; Hu, J.-S.; Wan, L.-J. Bandgap Engineering of Monodispersed $Cu_{2-x}S_ySe_{1-y}$ Nanocrystals through Chalcogen Ratio and Crystal Structure. *J. Am. Chem. Soc.* **2011**, *133*, 18558–18561.
12. Wang, J.-J.; Wang, Y.-Q.; Cao, F.-F.; Guo, G.-Y.; Wan, L.-J. Synthesis of Monodispersed Wurtzite $CuInSe_2$ Nanocrystals and Their Application in High-Performance Organic−Inorganic Hybrid Photodetectors. *J. Am. Chem. Soc.* **2010**, *132*, 12218–12221.
13. Schlecht, S.; Budde, M.; Kienle, L. Nanocrystalline Tin as a Preparative Tool: Synthesis of Unprotected Nanoparticles

of SnTe and SnSe and a New Route to $(PhSe)_4Sn$. *Inorg. Chem.* **2002**, *41*, 6001–6005.
14. Ruberu, T. P. A.; Vela, J. Expanding the One-Dimensional CdS–CdSe Composition Landscape: Axially Anisotropic $CdS_{1-x}Se_x$ Nanorods. *ACS Nano* **2011**, *5*, 5775–5784.
15. Alemseghed, M. G.; Ruberu, T. P. A.; Vela, J. Controlled Fabrication of Colloidal Semiconductor-Metal Hybrid Heterostructures: Site Selective Metal Photo Deposition. *Chem. Mater.* **2011**, *23*, 3571–3579.
16. Ruberu, T. P. A.; Albright, H. R.; Callis, B.; Ward, B.; Cisneros, J.; Fan, H.-J.; Vela, J. Molecular Control of the Nanoscale: Effect of Phosphine Chalcogenide Reactivity on CdS–CdSe Nanocrystal Composition and Morphology. *ACS Nano* **2012**, *6*, 5348–5359.
17. Ko, W. Y. L.; Bagaria, H. G.; Asokan, S.; Lina, K. J.; Wong, M. S. CdSe Tetrapod Synthesis Using Cetyltrimethylammonium Bromide and Heat Transfer Fluids. *J. Mater. Chem.* **2010**, *20*, 2474–2478.
18. Wang, W.; Geng, Y.; Qian, Y.; Ji, M.; Liu, X. A Novel Pathway to PbSe Nanowires at Room Temperature. *Adv. Mater.* **1998**, *10*, 1479–1481.
19. Xi, L.; Chua, K. H.; Zhao, Y.; Zhang, J.; Xiong, Q.; Lam, Y. M. Controlled Synthesis of CdE (E = S, Se and Te) Nanowires. *RSC Adv.* **2012**, *2*, 5243–5253.
20. Shen, H.; Wang, H.; Chen, X.; Niu, J. Z.; Xu, W.; Li, X. M.; Jiang, X.-D.; Du, Z.; Li, L. S. Size- and Shape-Controlled Synthesis of CdTe and PbTe Nanocrystals Using Tellurium Dioxide as the Tellurium Precursor. *Chem. Mater.* **2010**, *22*, 4756–4761.
21. Pang, Q.; Zhao, L.; Cai, Y.; Nguyen, D. P.; Regnault, N.; Wang, N.; Yang, S.; Ge, W.; Ferreira, R.; Bastard, G.; *et al.* CdSe Nanotetrapods: Controllable Synthesis, Structure Analysis, and Electronic and Optical Properties. *Chem. Mater.* **2005**, *17*, 5263–5267.
22. Yang, J.; Xue, C.; Yu, S. H.; Zeng, J. H.; Qian, Y. T. General Synthesis of Semiconductor Chalcogenide Nanorods by Using the Monodentate Ligand *n*-Butylamine as a Shape Controller. *Angew. Chem., Int. Ed.* **2002**, *41*, 4697–4700.
23. Govan, J. E.; Jan, E.; Qurejeta, A.; Kotov, N. A.; Gun'ko, Y. K. Chiral Luminescent CdS Nano-tetrapods. *Chem. Commun.* **2010**, *46*, 6072–6074.
24. Asokan, S.; Krueger, K. M.; Colvin, V. L.; Wong, M. S. Shape-Controlled Synthesis of CdSe Tetrapods Using Cationic Surfactant Ligands. *Small* **2007**, *3*, 1164–1169.
25. Manna, L.; Scher, E. C.; Alivisatos, A. P. Synthesis of Soluble and Processable Rod-, Arrow-, Teardrop-, and Tetrapod-Shaped CdSe Nanocrystals. *J. Am. Chem. Soc.* **2000**, *122*, 12700–12706.
26. Wang, F.; Buhro, W. E. Morphology Control of Cadmium Selenide Nanocrystals: Insights into the Roles of Di-*n*-octylphosphine Oxide (DOPO) and Di-*n*-octylphosphinic Acid (DOPA). *J. Am. Chem. Soc.* **2012**, *134*, 5369–5380.
27. Liu, H.; Tao, H.; Yang, T.; Kong, L.; Qin, D.; Chen, J. A Surfactant-Free Recipe for Shape-Controlled Synthesis of CdSe Nanocrystals. *Nanotechnology* **2011**, *22*, 045604.
28. Huang, J.; Kovalenko, M. V.; Talapin, D. V. Alkyl Chains of Surface Ligands Affect Polytypism of CdSe Nanocrystals and Play an Important Role in the Synthesis of Anisotropic Nanoheterostructures. *J. Am. Chem. Soc.* **2010**, *132*, 15866–15868.
29. Fiore, A.; Mastria, R.; Lupo, M. G.; Lanzani, G.; Giannini, C.; Carlino, E.; Morello, G.; De Giorgi, M.; Li, Y.; Cingolani, R.; *et al.* Tetrapod-Shaped Colloidal Nanocrystals of II–VI Semiconductors Prepared by Seeded Growth. *J. Am. Chem. Soc.* **2009**, *131*, 2274–2282.
30. Talapin, D. V.; Nelson, J. H.; Shevchenko, E. V.; Aloni, S.; Sadtler, B.; Alivisatos, A. P. Seeded Growth of Highly Luminescent CdSe/CdS Nanoheterostructures with Rod and Tetrapod Morphologies. *Nano Lett.* **2007**, *7*, 2951–2959.
31. Peng, X.; Manna, L.; Yang, W.; Wickham, J.; Scher, E.; Kadavanich, A.; Alivisatos, A. P. Shape Control of CdSe Nanocrystals. *Nature* **2000**, *404*, 59–61.
32. Peng, Z. A.; Peng, X. Nearly Monodisperse and Shape-Controlled CdSe Nanocrystals *via* Alternative Routes: Nucleation and Growth. *J. Am. Chem. Soc.* **2002**, *124*, 3343–3353.
33. Xie, R.; Kolb, U.; Basche, T. Design and of Colloidal Nanocrystal Heterostructures with Tetrapod Morphology. *Small* **2006**, *2*, 1454–1457.
34. Lim, J.; Bae, W. K.; Park, K. U.; Zur Borg, L.; Zentel, R.; Lee, S.; Char, K. Controlled Synthesis of CdSe Tetrapods with High Morphological Uniformity by the Persistent Kinetic Growth and the Halide-Mediated Phase Transformation. *Chem. Mater.* **2012**, 10.1021/cm3035592.
35. Zhang, W.; Jin, C.; Yang, Y.; Zhong, X. Noninjection Facile Synthesis of Gram-Scale Highly Luminescent CdSe Multipod Nanocrystals. *Inorg. Chem.* **2012**, *51*, 531–535.
36. Lutich, A. A.; Mauser, C.; Da Como, E.; Huang, J.; Vaneski, A.; Talapin, D. V.; Rogach, A. L.; Feldmann, J. Multiexcitonic Dual Emission in CdSe/CdS Tetrapods and Nanorods. *Nano Lett.* **2010**, *10*, 4646–4650.
37. Choi, C. L.; Li, H.; Olson, A. C. K.; Jain, P. K.; Sivasankar, S.; Alivisatos, A. P. Spatially Indirect Emission in a Luminescent Nanocrystal Molecule. *Nano Lett.* **2011**, *11*, 2358–2362.
38. Lee, D. C.; Robel, I.; Pietryga, J. M.; Klimov, V. I. Infrared-Active Heterostructured Nanocrystals with Ultralong Carrier Lifetimes. *J. Am. Chem. Soc.* **2010**, *132*, 9960–9962.
39. Bealing, C. R.; Baumgardner, W. J.; Choi, J. J.; Hanrath, T.; Hennig, R. G. Predicting Nanocrystal Shape through Consideration of Surface-Ligand Interactions. *ACS Nano* **2012**, *6*, 2118–2127.
40. Kumar, S.; Nann, T. Shape Control of II–VI Semiconductor Nanomaterials. *Small* **2006**, *2*, 316–329.
41. Manna, L.; Milliron, D. J.; Meisel, A.; Scher, E. C.; Alivisatos, A. P. Controlled Growth of Tetrapod-Branched Inorganic Nanocrystals. *Nat. Mater.* **2003**, *2*, 382–385.
42. Nourbakhsh, S.; Liao, C. L.; Ng, Y. G. A 193 nm Laser Photofragmentation Time-of-Flight Mass Spectrometric Study of CH_3SSCH_3, $SSCH_3$, and SCH_3. *J. Chem. Phys.* **1990**, *92*, 6587–6593.
43. McMillen, D. F.; Golden, D. M. Hydrocarbon Bond Dissociation Energies. *Annu. Rev. Phys. Chem.* **1982**, *33*, 493–532.
44. Luo, Y.-R. *Comprehensive Handbook of Chemical Bond Energies*; CRC Press: Boca Raton, FL, 2007; pp 425–454.
45. Benson, S. W. Thermochemistry and Kinetics of Sulfur-Containing Molecules and Radicals. *Chem. Rev.* **1978**, *78*, 23–35.
46. Płaza, S.; Gruziński, R. Homogeneous and Heterogeneous Thermal Decomposition of Diphenyl Disulphide. *Wear* **1996**, *194*, 212–218.
47. Mortimer, C. T.; Waterhouse, J. Enthalpy of Combustion of Diphenyl Diselenide. *J. Chem. Thermodyn.* **1980**, *12*, 961–965.
48. Arshadi, M. R.; Shabrang, M. Heats of Combustion and Formation of 4-Phenyl-1,2,3-selenadiazole and Dibenzyl Diselenide. *J. Chem. Soc., Perkin Trans. 2* **1973**, *2*, 1732–1734.
49. Benassi, R.; Taddei, F. Complete Basis Set Model Chemistry Applied to Molecules of Increasing Molecular Complexity: Thermochemical Properties of Organic Sulfur Derivatives. *J. Comput. Chem.* **2000**, *21*, 1405–1418.
50. Zou, L.-F.; Fu, Y.; Shen, K.; Guo, Q.-X. Sulfur–Sulfur Bond Dissociation Enthalpies: A High-Level *Ab Initio* Study. *THEOCHEM* **2007**, *807*, 87–92.
51. Zou, L.-F.; Shen, K.; Fu, Y.; Guo, Q.-X. Initiation of Petroleum Formation and Antioxidant Function—A DFT Study of Sulfur–Sulfur Bond Dissociation Enthalpies. *J. Phys. Org. Chem.* **2007**, *20*, 754–763.
52. Heverly-Coulson, G. S.; Boyd, R. J. Systematic Study of the Performance of Density Functional Theory Methods for Prediction of Energies and Geometries of Organoselenium Compounds. *J. Phys. Chem. A* **2011**, *115*, 4827–4831.
53. Gámez, J. A.; Yáñez, M. Asymmetry and Electronegativity in the Electron Capture Activation of the Se–Se Bond: σ^*(Se–Se) *vs* σ^*(Se–X). *J. Chem. Theory Comput.* **2010**, *6*, 3102–3112.
54. Yoffe, A. D. Low-Dimensional Systems: Quantum Size Efects and Electronic Properties of Semiconductor Microcrystallites (Zero-Dimensional Systems) and Some Quasi-Two-Dimensional Systems. *Adv. Phys.* **2002**, *51*, 799–890.
55. Wang, Y.; Herron, N. Nanometer-Sized Semiconductor Clusters: Materials Synthesis, Quantum Size Effects, and

Photophysical Properties. *J. Phys. Chem.* **1991**, *95*, 525–532.
56. Fonoberov, V. A.; Pokatilov, E. P.; Mateevici, A. Exciton States and Optical Transitions in Colloidal CdS Quantum Dots: Shape and Dielectric Mismatch Effects. *Phys. Rev. B* **2002**, *66*, 085310.
57. Smith, A. M.; Nie, S. Semiconductor Nanocrystals: Structure, Properties, and Band Gap Engineering. *Acc. Chem. Res.* **2010**, *43*, 190–200.
58. Doll, J. D.; Hu, B.; Papadimitrakopoulos, F. Precursor and Oxygen Dependence of the Unidirectional, Seeded Growth of CdSe Nanorods. *Chem. Mater.* **2012**, *24*, 4043–4050.
59. Yu, W. W.; Qu, L.; Guo, W.; Peng, X. Experimental Determination of the Extinction Coefficient of CdTe, CdSe, and CdS Nanocrystals. *Chem. Mater.* **2003**, *15*, 2854–2860; **2004**, *16*, 560.
60. Jasieniak, J.; Smith, L.; van Embden, J.; Mulvaney, P.; Califano, M. Re-examination of the Size-Dependent Absorption Properties of CdSe Quantum Dots. *J. Phys. Chem. C* **2009**, *113*, 19468–19474.
61. Capek, R. K.; Moreels, I.; Lambert, K.; De Muynck, D.; Zhao, Q.; Van Tomme, A.; Vanhaecke, F.; Hens, Z. Optical Properties of Zincblende Cadmium Selenide Quantum Dots. *J. Phys. Chem. C* **2010**, *114*, 6371–6376.
62. Leatherdale, C. A.; Woo, W.-K.; Mikulec, F. V.; Bawendi, M. G. On the Absorption Cross Section of CdSe Nanocrystal Quantum Dots. *J. Phys. Chem. B* **2002**, *106*, 7619–7622.
63. Guo, Y.; Marchuk, K.; Sampat, S.; Abraham, R.; Fang, N.; Malko, A.; Vela, J. Unique Challenges Accompany Thick-Shell CdSe/*n*CdS ($n > 10$) Nanocrystal Synthesis. *J. Phys. Chem. C* **2012**, *116*, 2791–2800.
64. Schmidt, M. W.; Baldridge, K. K.; Boatz, J. A.; Elbert, S. T.; Gordon, M. S.; Jensen, J. S.; Koseki, S.; Matsunaga, N.; Nguyen, K. A.; Su, S.; *et al.* General Atomic and Molecular Electronic-Structure System. *J. Comput. Chem.* **1993**, *14*, 1347–1363.
65. Gordon, M. S.; Schmidt, M. W. Advances in Electronic Structure Theory: GAMESS a Decade Later. In *Theory and Applications of Computational Chemistry: The First Forty Years*; Dykstra, C. E., Frenking, G., Kim, K. S., Scuseria, G. E., Eds.; Elsevier Science: Amsterdam, 2005; p 1167.
66. Hehre, W. J.; Ditchfield, R.; Pople, J. A. Self-Consistent Molecular Orbital Methods. XII. Further Extensions of Gaussian-Type Basis Sets for Use in Molecular Orbital Studies of Organic Molecules. *J. Chem. Phys.* **1972**, *56*, 2257–2261.
67. Boese, A. D.; Martin, J. M. L. Development of Density Functionals for Thermochemical Kinetics. *J. Chem. Phys.* **2004**, *121*, 3405–3416.
68. Denk, M. K. The Variable Strength of the Sulfur−Suflur Bond: 78 to 41 kcal—G3, CBS-Q and DFT Bond Energies of Sulfur (S_8) and Disulfanes XSSX (X = H, F, Cl, CH_3, CN, NH_2, OH, SH). *Eur. J. Inorg. Chem.* **2009**, 1358–1368.
69. Bode, B. M.; Gordon, M. S. MacMolPlt: A Graphical User Interface for GAMESS. *J. Mol. Graphics Modell.* **1998**, *16*, 133.
70. Ditchfield, R.; Hehre, W. J.; Pople, J. A. Self-Consistent Molecular-Orbital Methods. IX. An Extended Gaussian-Type Basis for Molecular-Orbital Studies of Organic Molecules. *J. Chem. Phys.* **1971**, *54*, 724–728.
71. Krishnan, R.; Binkley, J. S.; Seeger, R.; Pople, J. A. Self-Consistent Molecular Orbital Methods. XX. A Basis Set for Correlated Wave Functions. *J. Chem. Phys.* **1980**, *72*, 650–654.
72. Mitin, A. V.; Baker, J.; Pulay, P. An Improved 6-31G(*) Basis Set for First-Row Transition Metals. *J. Chem. Phys.* **2003**, *118*, 7775–7782.
73. Roothaan, C. C. J. New Developments in Molecular Orbital Theory. *Rev. Mod. Phys.* **1951**, *23*, 69–89.